Large-scale cloud, precipitation, and upper level features during Fronts and Atlantic Storm Track Experiment as inferred from TIROS-N Operational Vertical Sounder observations

Jean-pierre Chaboureau, Chantal Claud, Jean-pierre Cammas, Patrick Mascart

JOURNAL OF GEOPHYSICAL RESEARCH, VOL. 106, NO. D15, PAGES 17,293–17,302, AUGUST 16, 2001

Large-scale cloud, precipitation, and upper level features during Fronts and Atlantic Storm Track Experiment as inferred from TIROS-N Operational Vertical Sounder observations

Jean-Pierre Chaboureau
Laboratoire d'Aérologie, Toulouse, France

Chantal Claud
Laboratoire de Météorologie Dynamique, Palaiseau, France

Jean-Pierre Cammas and Patrick J. Mascart
Laboratoire d'Aérologie, Toulouse, France

Abstract. Physical parameters retrieved from the measurements of the TIROS-N Operational Vertical Sounder aboard the National Oceanic and Atmospheric Administration satellites are used to study the large-scale cloud, precipitation, upper level features during the Fronts and Atlantic Storm Track Experiment period: the cloud top pressure, a precipitation index, and the temperature of lower stratosphere (TLS), respectively. The three dynamically consistent (i.e., temporally and spatially collocated) retrievals are able to characterize the weather regimes through their organization in locations expected from the cyclonic activity. Moreover, high-level cloud patterns, when accompanied by rain, can be discriminated with respect to TLS field. When no (or weak) warm TLS feature can be found upstream, such patterns are frontal systems. On the contrary, a warm TLS event present upstream of a rainy cloud feature suggests a baroclinic interaction. In this case, the high-level cloud pattern is associated with a large-scale baroclinic cyclone, or at least a mature low. When examining the most precipitating cases using a composite technique, the nondeveloped systems (in term of absence of high-cloud cover) are characterized by the absence of warm TLS features, grouping mostly blocking-regime cases. On the other hand, the cases that are well developed in terms of cloud cover are characterized by warm TLS patterns upstream the precipitation area. Moreover, the well-developed cases could be grouped into three families depending on the orientation of the warm TLS features: zonal, anticyclonic, and cyclonic. Only the later family, characterized by a cyclonically tilted trough, clusters the large-scale baroclinic systems that all occurred during the zonal regime. This suggests that a cyclonically tilted trough has a positive impact on the development of cyclones.

1. Introduction

Extratropical cyclones prediction remains a challenge for western European meteorology due to the difficulty to forecast damaging weather, resulting from strong winds and heavy rainfalls. Serious forecast failures associated with intense atmospheric development are often thought to be due more to localized errors in sensitive areas of the initial conditions [*Szunyogh et al.*, 1999] than to model deficiencies [*Lorenz*, 1990]. Some recent investigations with data assimilation systems find these sensitive areas in proximity to a lowered tropopause in regions of strong thermal gradients below the main concentration of potential vorticity in the upper troposphere [*Langland et al.*, 1999; *Gelaro et al.*, 1999].

Seen from a more theoretical perspective, an important issue is the extratropical cyclones mechanism of development, which is classically pictured by the baroclinic instability model [*Charney*, 1947; *Eady*, 1949] in which an upper level potential vorticity anomaly upstream interacts with a low-level baroclinic region [*Hoskins et al.*, 1985]. Examining the significance of upper level potential vorticity anomalies for the growth of observed cyclogenesis events was one of the many objectives of the Fronts and Atlantic Storm Track Experiment (FASTEX), which included 19 Intensive Observing Periods (IOPs) and sampled 25 cyclone life cycles in January and February 1997 [*Joly et al.*, 1997, 1999]. The FASTEX sample largely confirms the relevance of upper level potential vorticity anomalies in cyclone de-

Paper number 2000JD000150.
0148-0227/01/2000JD000150$09 00

velopment but suggests that real cyclones often have complex life cycles in response to multiple transient baroclinic interaction phases. In this mechanism an upper level potential vorticity anomaly approaches a low-level baroclinic region, leads to a transient phase of development, but instead of locking in phase with the low-level feature, departs from it in the subsequent evolution [*Baehr et al.*, 1999] . A baroclinic development occurs as a transient response to the upper level anomaly forcing, but the distinctive phase locking of the classical baroclinic instability model is missing. This mechanism is also supported by the climatological study of 14 reanalyzed winters of *Ayrault and Joly* [2000] which shows that the significant cyclogenesis events (deepening greater than 10 hPa per day) always involve a transient baroclinic interaction with some upper level potential vorticity anomaly.

Another novel aspect from FASTEX comes from the study of two large-scale cyclones (IOP11 and IOP17) by *Kucharski and Thorpe* [2000], showing that barotropic energy conversion dominates the initial phase of the development of these cyclones, prior to the further baroclinic conversion. A further idealized study shows that the backward tilt (against the shear) of an upper level trough approaching the jet associated with a baroclinic zone serves as the most favorable situation for the barotropic growth of the trough [*Kucharski and Thorpe*, 2001]. Although this idealized study does not consider the change in orientation of the trough by the cyclonic flow, this emphasizes the role and the orientation of the trough.

Furthermore, the importance of the trough orientation in cyclone development has been characterized through simulations with the addition of a meridional barotropic wind shear to a baroclinic flow [e.g., *Thorncroft et al.*, 1993; *Shapiro et al.*, 1999]. Cyclones evolving in a non sheared environment (referred to as Life Cycle 1; LC1) are characterized by backward tilted, thinning troughs being advected anticyclonically and equatorward. They develop into T-bone bent-back warm-frontal cyclones. The cyclones evolving in a cyclonically sheared environment (referred to as Life Cycle 2; LC2) are characterized by forward tilted, broadening troughs wrapping themselves up cyclonically and poleward and mature into classical Norwegian occluded cyclones. Recently, *Shapiro et al.* [2001] have linked these idealized simulations with life cycles over the eastern North Pacific. They have suggested that anomalies in the time-mean ambient flow associated during El Niño and La Niña episodes lead to preferential baroclinic life cycles that mimic the idealized LC1 and LC2 paradigms, respectively.

Up to now these climatological studies investigating the role of the upper level trough in the development of storms were based on the use of either analysis or model forecasts, yielding to examine some dynamical variables (essentially wind and temperature). The satellite observation affords us a long-time archive on storms, as seen through their signature on the water budget (cloud and precipitation). In particular, the infrared and microwave data from the TIROS-N Operational Vertical Sounder (TOVS) is useful for retrievals of atmospheric, cloud, precipitation, and surface parameters [*Smith et al.*, 1979]. Among them the cloud cover and the rain index allow us to select the most significant weather systems while the temperature of lower stratosphere (TLS) [*Fourrié et al.*, 2000] characterizes the tropopause level thermal patterns.

To get suitable information on precipitation, we develop a new calibration procedure for the rain index using the microwave sounding unit (MSU) data. Section 2 presents the retrieval of the physical parameters from the TOVS data. Then we investigate the organization between the distributions of the satellite retrievals, with respect to the baroclinic interaction. This is done over the FASTEX period, helped by a large amount of earlier dynamical work done on this experiment. Section 3 describes the results, first by looking at the mean distributions, then by using Hovmöller diagrams, and finally by investigating the most intense rain events through a composite technique. In particular, we examine whether a preferential distribution of cloud field can show up within the TLS distribution and whether it could mimic one of the life cycle paradigms cited above. Section 4 concludes the paper.

2. Retrieval of Physical Parameters From TOVS Data

The TOVS instrument flies aboard the National Oceanic and Atmospheric Administration (NOAA) series of operational polar satellites since 1979. Observations used here are from NOAA 12, that is at 0600 and 1800 UTC over the North Atlantic. The raw TOVS data are converted into atmospheric parameters using the Improved Initialization Inversion (3I) algorithm [*Chédin et al.*, 1985; *Scott et al.*, 1999]. This physicostatistical method, relying on pattern recognition, determines the following parameters: air mass type, temperature and water vapor profiles, cloud heights, amounts and types, and surface parameters (temperature and emissivity). For a full description of the method the reader is referred to *Chédin et al.* [1985] and *Scott et al.* [1999]. In the following subsections we detail the method for retrieving the temperature of lower stratosphere (TLS), the cloud top pressure, and the precipitation index. All these variables are retrieved in each 3I box with a spatial resolution of 100 km by 100 km, a compromise between the spatial resolution of the High-Resolution Infrared Radiation Sounder (HIRS) and the MSU, which are the main components of the TOVS. The characteristics of the TOVS channels used in this study are listed in Table 1.

2.1. Temperature of Lower Stratosphere

The temperature of lower stratosphere (TLS) [see *Chédin et al.*, 1985] is used to describe the thermal structures at the tropopause level [*Fourrié et al.*, 2000]. TLS is obtained through a combination of brightness temperatures from five TOVS channels (HIRS 2 and 3; MSU 2, 3, and 4) weighted by a set of regression coefficients. These TOVS channels are the most sensitive to the temperature around the tropopause.

Table 1. Characteristics of the TOVS Channels Used in This Study[a]

Name	Central Wavelength or Frequency[b]	Principal Absorbing Constituents	Level of Peak Energy Contribution, hPa
HIRS 2	14.70	CO_2	60
HIRS 3	14.50	CO_2	100
HIRS 4	14.20	CO_2	400
HIRS 5	14.00	CO_2	600
HIRS 6	13.70	CO_2/H_2O	800
HIRS 7	13.40	CO_2/H_2O	900
HIRS 8	11.10	window	surface
MSU 1	50.31	window	surface
MSU 2	53.73	O_2	700
MSU 3	54.96	O_2	300
MSU 4	57.95	O_2	90

[a]Adapted from *Smith et al.* [1979].
[b]Wavelength (μm) for HIRS and frequency (GHz) for MSU.

While MSU3 plays the major role, the other channels are also significant. As a consequence, TLS fields show more variability than the raw MSU3 data alone.

As shown through quantitative comparisons with model analysis, TLS is a good indicator of the averaged temperature between the 4 and 8 PVU (potential vorticity unit, 1 PVU = 10^{-6} K m^2 s^{-1} kg^{-6}) levels (i.e., in the layer 1-4.5 km above the tropopause). In particular, warm anomalies of TLS can be used to detect upper level precursors. Moreover, TLS fields allow to detect other upper level structures such as troughs, ridges, and tropopause breaks along the cyclonic shear side of an upper level jet [*Fourrié et al.*, 2000].

2.2. Cloud Top Pressure

In the 3I algorithm, clouds are detected at the HIRS spatial resolution (18 km at nadir) by a succession of 7 (night)/8 (day) threshold tests, which depend on the simultaneous MSU radiance measurements probing through clouds. Cloud parameters are determined from the radiances averaged over all cloudy HIRS pixels within the 3I box, assuming a single, homogeneous cloud layer. The average cloud top pressure and the effective cloud amount are obtained by a weighted-χ^2 method from four 15 μm CO_2 band radiances and the 11 μm atmospheric window radiance (HIRS 4 to 8) [*Stubenrauch et al.*, 1999b]. The empirical weights reflect the usefulness of a spectral channel at a cloud level for the determination of the effective cloud amount. A cloud cover fraction is also determined as the fraction of cloudy HIRS pixels in each grid box. The 3I cloud parameters have been evaluated on a global scale [*Stubenrauch et al.*, 1999a] by comparison with time-space collocated, reprocessed International Satellite Cloud Climatology Project (ISCCP) cloud parameters [*Rossow et al.*, 1996]. The remaining discrepancies with ISCCP can be explained by differences in cloud detection sensitivity, differences in the atmospheric temperatures profiles used, and by inhomogeneous or partly cloudy fields.

2.3. Precipitation Flag

The MSU is a four-channel passive microwave radiometer for which the horizontal resolution is ranging from 110 km at nadir to 323 km at the edges of the swath. In spite of its rather coarse resolution with respect to mesoscale features, the MSU gives us valuable information on precipitation which has the advantage to be collocated with the other geophysical variables we study, that is TLS and the cloud top pressure. In particular, MSU1 and MSU2 sense upwelling radiation at 50.31 and 53.73 GHz, respectively, with respective peak responses at sea level and 700 hPa. MSU2 has its primary signal due to absorption and emission of thermal radiation by molecular oxygen. In contrast to MSU2, MSU1 experiences large cloud water and surface contributions compared to its air temperature sensitivity. Thus in mid-February 1980 an oceanic precipitation test was introduced operationally by the National Environmental Satellite Service. It consisted of declaring situations contaminated by rain when the brightness temperature (BT) difference of MSU2 minus MSU1 is less than 12 K [*Phillips*, 1980]. In the 3I algorithm the same test on MSU data is used, but with a threshold set at 16 K [e.g., *Claud et al.*, 1995]. (Note that *Spencer* [1993] has gone further in the use of the MSU data, by developing a sophisticated algorithm to retrieve the rain rate. Using a simple threshold to detect rain is sufficient here and easier to implement.)

An example of difference of MSU2 minus MSU1 (hereinafter ΔMSU) is presented in Figure 1a at 1800 UTC February 18, 1997. Due to large signal either from land or sea ice, the difference field is only plotted over open ocean. Two centers of low values of ΔMSU, less than 18 K, indicate the locations of the wave centers during the FASTEX IOP17, around (25°W, 50°N) and (32°W, 43°N). This test on ΔMSU is thus a good indicator of rain there. But the large values of ΔMSU found between these two minimum centers (around 30°W and between 40°N and 50°N) suggest a non precipitating area in the frontal zone that seems to be unrealistic. Elsewhere, ΔMSU tends to display smaller values at nadir than at limb (see, e.g., the part of the swath south of 40°N, between 28°W and 10°W).

It is worth noting that the MSU data from NOAA in this study are corrected for the effect of scan angle. The limb correction procedure for the MSU channels corrects not only for limb effects but also for several other factors in the case of MSU2 that affect the actual microwave measurements, including precipitating clouds, variable surface emissivity, and sidelobes in the antenna pattern [*Koehler*, 1989]. Results from Figure 1a suggest that this procedure is not completely successful.

To correct these uncontrolled effects of the correction procedure and to obtain a well-calibrated precipitation flag from MSU, we use additional microwave observations taken at a fixed viewing angle. They come from the Special Sensor Microwave/Imager (SSM/I) aboard the Defense Meteorological

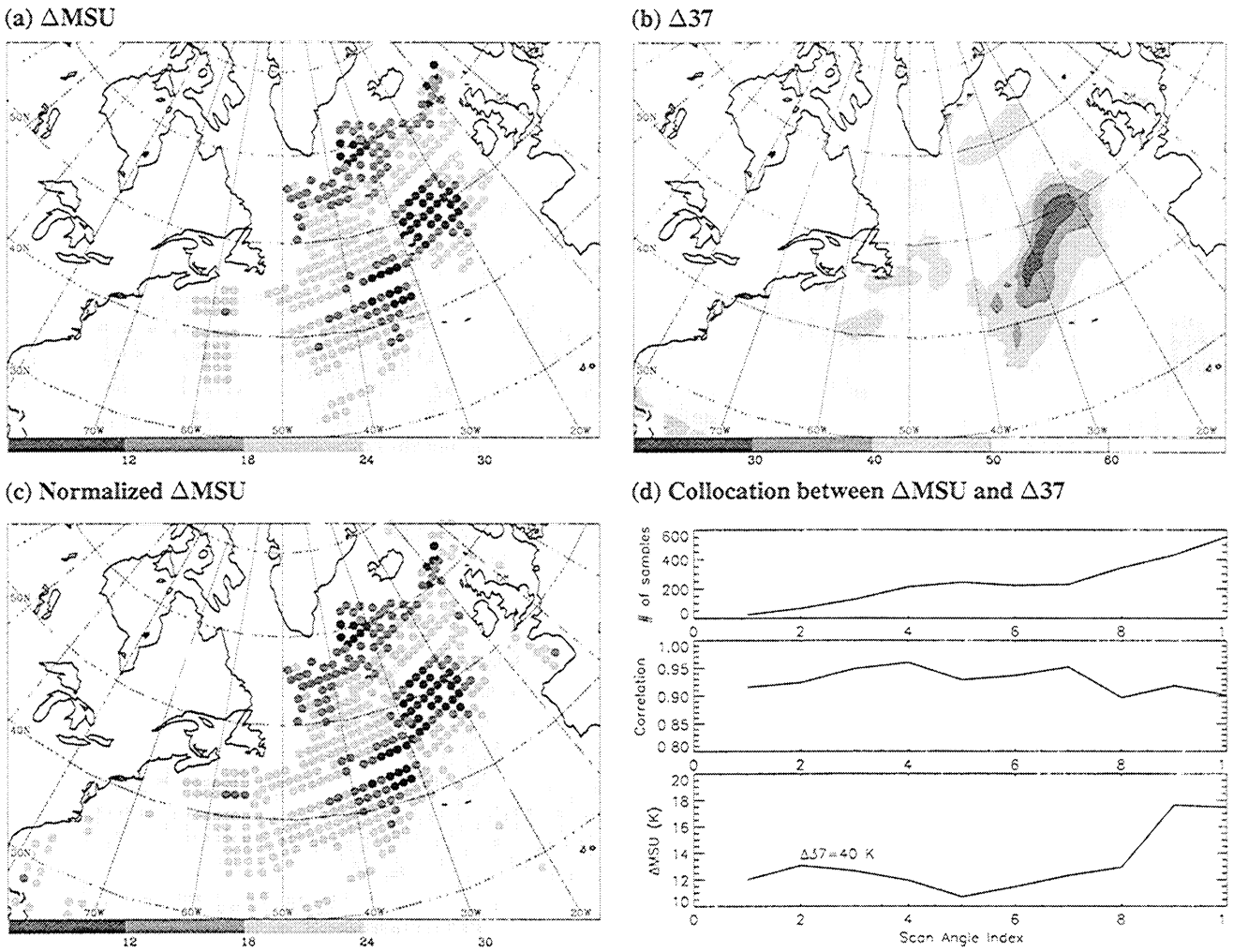

Figure 1. Maps at 1800 UTC February 18, 1997 of (a) ΔMSU (Kelvin), (b) Δ37 (Kelvin), (c) normalized ΔMSU (Kelvin). (d) Results, for the FASTEX period, of the collocation between ΔMSU and Δ37 according to the scan angle index of the 3I box. From top to bottom, number of samples, correlation, and correspondence of $\Delta 37 = 40$ K with ΔMSU.

Satellite Programme series. In particular, the polarization difference of the BTs at 37 GHz (vertically minus horizontally polarized BT; hereinafter Δ37) is attenuated by rain cloud and thus provides a simple and robust test to detect precipitation areas. Comparisons with ground-based radars suggest that a good indicator of rain over water in the tropics and subtropics is a Δ37 value less than 40 K. Higher-latitude studies should allow for larger polarization differences before rain is deemed unlikely [*Kummerow and Giglio*, 1994]. Figure 1b displays the 37 GHz BT polarization difference at 1800 UTC February 18, 1997. One can see the obvious correlation that could exist between ΔMSU and Δ37, if the limb effects on ΔMSU could be removed.

For this purpose the SSM/I observations have been collocated with the MSU data over the FASTEX period. The space-time window is 120 km (which roughly corresponds to the 3I box size) and 10 min (due to the high temporal variability of rain). The results of the comparison between ΔMSU and Δ37 are presented according to the scan angle index of the 3I box (Figure 1d).

Due to the rather narrow collocation window in time, the number of samples is limited, from less than 50 at nadir to around 600 for the larger scan angle. However, a high correlation is found between ΔMSU and Δ37, almost over 0.90 everywhere. Therefore the matching between the threshold for Δ37 and the equivalent one for ΔMSU can be taken with a high level of confidence. The lowermost part of Figure 1d shows the ΔMSU threshold that gives the same 40 K Δ37 threshold. It permits us to normalize ΔMSU with respect to nadir. The normalized ΔMSU is obtained by multiplying ΔMSU by the fraction of the ΔMSU threshold corresponding to $\Delta 37 = 40$ K at nadir over the one at the scan angle of the observation.

Figure 1c presents ΔMSU after normalization. The uncontrolled effects of the limb correction have been removed. The normalized ΔMSU displays more homogeneous values between the two centers of minimal values. Also, in no-rain areas the difference between ΔMSU at nadir and ΔMSU to the limb have been reduced. In the following we use the threshold of 12 K for the normalized ΔMSU that corre-

sponds to a threshold of 40 K for $\Delta 37$ to detect precipitation areas.

3. Results

Variables retrieved as explained in section 2 are now used to investigate the large-scale properties of cloud, precipitation and upper level features during the FASTEX period. This is done first by looking at the mean distributions, then by using Hovmöller diagrams, and finally by investigating the most intense rain events through a composite technique.

3.1. Mean Distributions

To examine the mean distribution of the retrievals, we separate the FASTEX period into three distinct periods corresponding to the dynamical regimes found by *Joly et al.* [1999]: a Greenland anticyclone regime from January 1 to 13, followed by a blocking regime from January 14 to February 2, and finally a zonal regime during the rest of February. Averaged retrieval fields for the three regimes are displayed in Figure 2.

During the Greenland anticyclone regime, some maximum TLS areas, with values greater than 220 K, are located over North America and the western Atlantic Ocean as far as 40°W (Figure 2a). Due to the correspondence between TLS and the averaged temperature between 4 and 8 PVU levels found by *Fourrié et al.* [2000], this suggests that, in average, the upper level jet is located to the south of the warm core of TLS, where the gradient is strong. This interpretation is in agreement with the 300 hPa wind map displayed by *Joly et al.* [1999]. The cloud top pressure varies between 550 and 750 hPa over the North Atlantic (Figure 2d). Despite this small variation, the low values of cloud top pressure over the ocean are organized as a Y rotated counterclockwise. A similar organization is found for the densities of cyclone trajectories for January by *Baehr et al.* [1999]. Indeed, the high-level clouds are largely a result of the cyclone activities. The spatial variation of the normalized ΔMSU is small (Figure 2g).

During the blocking regime, maximum TLS areas display smaller values than for the two other regimes, with no mean values greater than 220 K (Figure 2b). The TLS pattern is also characteristically located just in the vicinity of the continents. Such an absence of the upper level jet over the ocean explains the weak organization of the mean distribution of the cloud top pressure (Figure 2e). An exception to

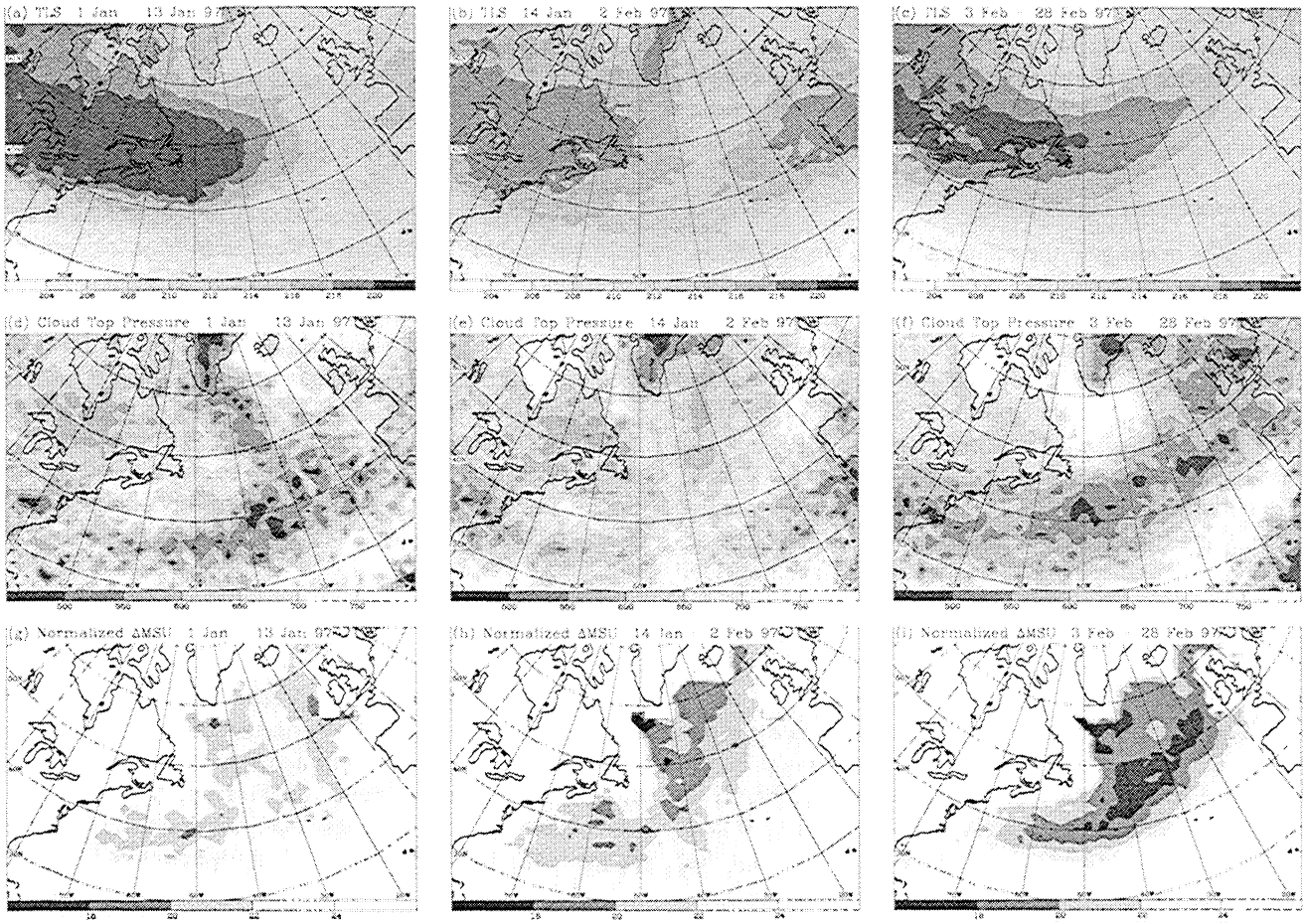

Figure 2. (a,b,c) Averaged fields of TLS (Kelvin), (d,e,f) cloud top pressure (hPa), and (g,h,i) normalized ΔMSU (Kelvin). The period of averaging is (left) from January 1 to 13, 1997, (middle) from January 14 to February 2, 1997, and (right) from February 3 to 28, 1997.

this statement is the meridional minimum at 30°W, where more high-level clouds are present, associated with a larger precipitation attenuation (Figure 2h).

During the zonal regime in February, the pattern of TLS (Figure 2c) is more elongated compared to the two other regimes of January. Averaged values of TLS larger than 218 K extend to 20°W, in a zone almost parallel to the 50°N. This indicates the presence of an elongated jet over the North Atlantic, just south of the TLS maximum area, that is, around 45°N. The cloud top pressure (Figure 2f) shows a region of low values from south of Newfoundland to the Norwegian Sea, in a direction rotated cyclonically with respect to the warm TLS axis. This cloud top pressure pattern is similar to a typical storm track of the zonal regime. The normalized ΔMSU displays minimum values, largely smaller than for January, and into two preferred locations (Figure 2i). First, rain activity is present south of Greenland, between 50°N and 60°N; due to strong surface air-sea exchanges in the Labrador Sea, this region is convectively unstable at low level. Second, a large precipitation area is located in the western part of the storm track, with a direction comparable to the cloud top pressure minimum one, that is, curved compared to the zonal pattern of TLS. This area of low values of the normalized ΔMSU ends just downstream the zone of TLS larger than 218 K.

In conclusion, the mean distributions of these satellite retrievals are organized in locations expected from the cyclonic activity. It demonstrates the capability of these particular retrieved fields to characterize the different weather regimes.

3.2. Hovmöller Diagrams

We now investigate the relationship, at large scale, between TLS, the cloud top pressure, and the normalized ΔMSU. These retrievals are averaged between 40°N and 60°N and plotted into Hovmöller diagrams (Figure 3). On the rightmost time axis, each IOP is marked, even if no TOVS data are available (IOP 8, 9, 10, and 11) or if the case is too north, like the cold-air cyclones (IOP 4 and 18). The subjective classification of the IOPs given by *Joly et al.* [1999] is used (large-scale baroclinic, end-of-storm track, comma clouds and cold-air cyclones; see caption of Figure 3). In addition, the warm anomalies of TLS and the cloud top pressure centers associated to the IOPs are identified at each time step and reported with lines on the diagrams, when meaningful (i.e., mostly for the cases of large-scale baroclinic cyclone).

The sharp contrast between the three different regimes seen in the previous section is also clear in Figure 3. Until January 13, the cloud top pressure minima are mainly located to the east of 50°W, representing two episodes of small frontal activities, with no (or, for IOP1, transient) associated upper level features. During the blocking regime, only two large-scale lows display high-level clouds associated with warm TLS upstream. The first one is IOP3, located in the eastern Atlantic on January 15, and the next one is found off the northeast coast of United States on January 26. Between these two dates, several fronts that are particularly characterized by an almost north-south orientation, slowly travel the ocean with no upper level features (IOP5 and 6) or with a narrow and weak trough (IOP7). From February 7 onwards a succession of extratropical cyclones (IOPs 12, 13, 14, 15, 16, 17, and 19) develop as the jet is installed over the ocean. Thus TLS displays a succession of warm and cold episodes, much more intense and rapid than in January. The troughs move eastward with a typical phase speed of 15° per day in February (to be compared with 10° per day only in January). (At 50° of latitude, this corresponds to a speed of 11.1 and 7.4 m s^{-1}, respectively.) The cloud top pressure and the normalized ΔMSU patterns are also more disturbed during the zonal regime than during the Greenland anticyclone and the blocking regime. In particular, their minimum patterns are all associated with a warm TLS feature upstream.

In summary, high-level cloud patterns, when accompanied by low values of normalized ΔMSU, can be discriminated with respect to the TLS field. When no (or weak) warm TLS feature can be found upstream, such patterns are frontal systems. On the contrary, a warm TLS event that is present upstream the rainy cloud feature suggests, at this scale, a baroclinic interaction. In this case, the high-level cloud pattern is associated with a large-scale baroclinic cyclone, or at least a mature low.

3.3. Composite Technique

To go further into the relationship between TLS, the cloud top pressure, and the normalized ΔMSU, we now focus on the events with the largest precipitation signature by using a composite method. The precipitation events are defined by areas covering more than 200,000 km^2 with values of the normalized ΔMSU less than 12 K. It leads to the selection of 67 organized systems, either fronts or cyclones at different stages of development. The selected large-rain events are framed by rectangular boxes, in the Hovmöller diagram of the normalized ΔMSU (right panel of Figure 3).

In the next stage, TLS, cloud top pressure, and normalized ΔMSU fields are extracted in a box of 3600 km side length. The orientation of the box is such as the Y axis is toward the north. To enlarge the view upstream of the rain event, the box is shifted 600 km to the east from the geometric center of the box. As normalized ΔMSU is also sensitive to low-level temperature variation (when normalized ΔMSU is over 40 K), we only use the fields of TLS and cloud top pressure in the following. Each case is thus represented by a vector of 31 x 31 x 2 = 1922 values. A reduction of space is necessary to classify the cases. A principal component analysis is thus performed on the normalized fields of TLS and the cloud top pressure in order to retain the pertinent information. Table 2 displays the results of the explained variance by the first 10 eigenvectors. The first eigenvectors represent the larger variance, but not necessarily a sufficient diversity of the cases. On the other hand, the eigenvectors of larger ranks describe lesser variance, associated with small-scale structures. A right place to separate into informative eigenvectors and useless ones is between the eigenvector of rank 6

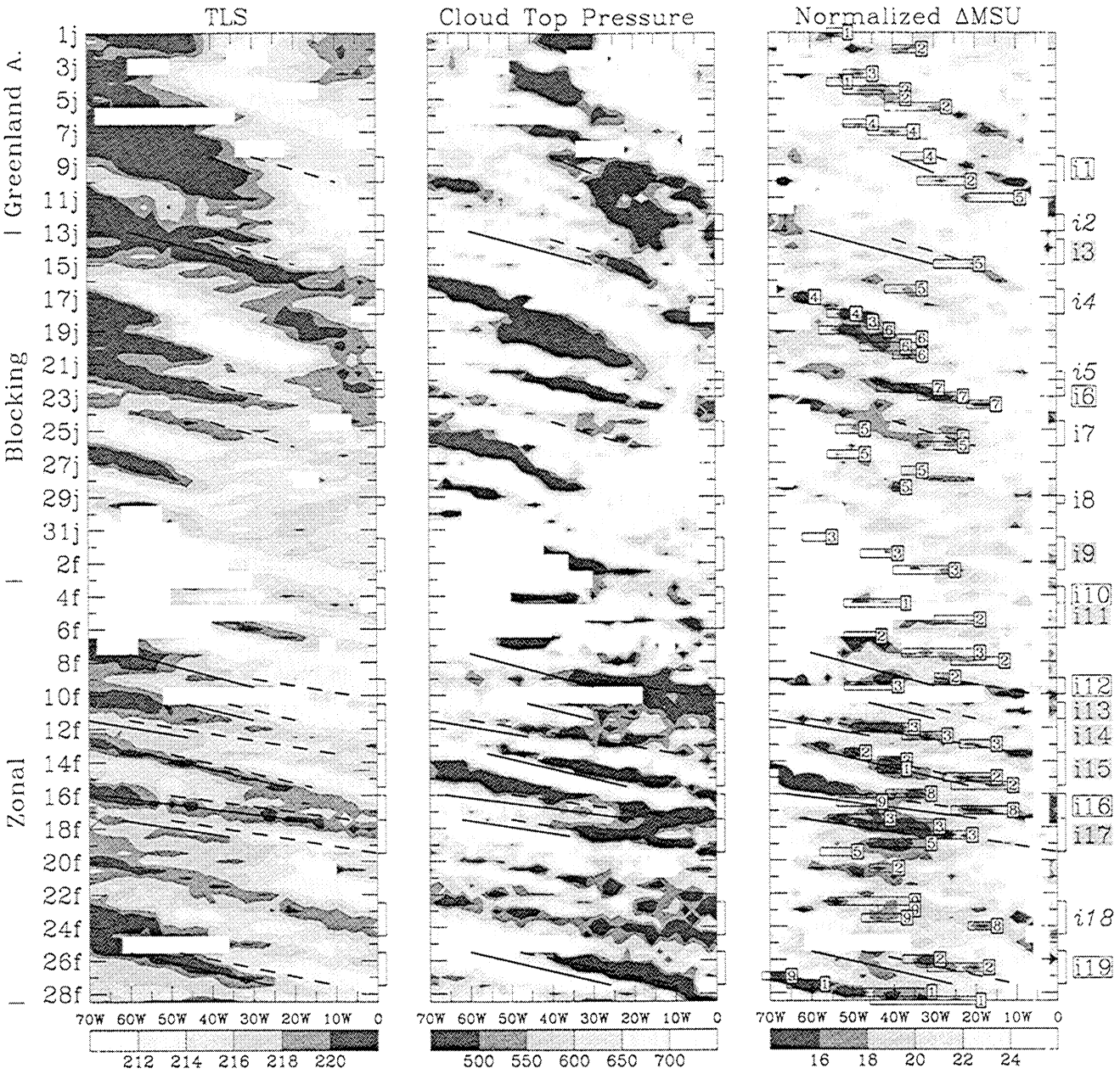

Figure 3. Hovmöller diagrams showing the longitude-time evolution of TLS (Kelvin), the cloud top pressure (hPa), and the normalized ΔMSU (Kelvin). On the left axis the scale indicates the day; j, January; f, February. On the right axis the symbols indicate the FASTEX IOPs: large-scale baroclinic cyclones are in the shadow box, end of storm track cyclones are in the clear box, comma clouds and cold-air cyclones are in italic. Solid (dashed) lines represent TLS (cloud top pressure) associated to IOPs. In the diagram related to the normalized ΔMSU, the boxes indicate the events examined with the composite analysis. The associated number is the class number at which the event belongs. See text related to composite for further details.

and of rank 7: there is a large decrease of the explained variance (1.30%) and the first six components represent 50.95% of the total variance.

Then the components kept are clustered using an ascending hierarchical classification, which minimizes the intraclass variance: each case is then included in a class. The key idea here, in the final step, is to generate the composite from averaging the original fields within each class, not the restricted subset of the principal components. This yields smooth but realistic structures as illustrated below. The retained classification gives nine classes. Indeed, to be representative, each class should be composed of a large number of individual cases (which is hard to obtain with an initial set of 67 events). On the other hand, a too limited number of classes would smooth the variability. Thus a satisfactory compromise is obtained with nine classes. Some of them only includes a few number of cases (less than five for classes 4, 6, 7, 8, and 9) due to the short period of time ana-

Table 2. Results of the Principal Component Analysis for the First 10 Eigenvectors

Rank	Explained Variance, %	Summation, %	Difference With the Variance Explained by the Next Rank %
1	19 23	19.23	9.76
2	9.48	28.71	2.85
3	6.63	35.34	0 63
4	5.99	41.33	0.87
5	5.12	46.46	0.63
6	4.49	50.95	1.30
7	3.20	54.15	0.38
8	2.82	56.97	0.41
9	2.41	59.38	0.06
10	2.35	61.74	0.11

lyzed. If a longer period would be studied, we might expect that the classes would be more populated, thus more representative. The number of the class at which each individual rain event belongs is plotted on Figure 3, next to each rectangular box. The averages of the composite fields within each class are shown in Figure 4.

Only one class (class 5) is characterized by middle-level clouds covering the precipitating area (Figure 4e). Moreover, the warm TLS pattern there is the weakest of all the classes. It is located to the southwest of the rainy area, that is, where no baroclinic interaction with the low levels is possible. Class 5 clusters 11 frontal cases, almost all occurring during the blocking regime.

All the other classes present high-level clouds over the precipitation area, with patterns of warm TLS upstream. For all these classes this suggests a baroclinic interaction between upper and low levels. Three families of classes could be identified according to the orientation of the warm TLS field: zonal, anticyclonic, and cyclonic.

The zonal family formed by classes 4, 8, and 9 presents warm fields of TLS organized in a zonal band north of the rain area (Figures 4d, 4h, and 4i). The high-level cloud patterns are elongated along this TLS zonal band. Classes 4 and 9 are populated by fronts located between 40°N and 45°N occurring in January and February, respectively (Figures 4d and 4i). Class 8 is characterized by a cloud shield composed by clouds higher and more cyclonically curved than the two other classes (Figure 4h). Indeed, class 8 is composed of three frontal waves (IOP 16 and Lesser Observing Period (LOP) 6) that develop into cyclones as the systems cross the jet stream from the warm to the cold-air side [*Baehr et al.*, 1999].

The anticyclonic family, that groups classes 6 and 7 (Figures 4f and 4g), is characterized by a warm TLS pattern located almost everywhere in the western part of the box, and in particular, anticyclonically curved for class 7. The high-level cloud patterns are elongated downstream of this TLS band. Class 6 concerns fronts during the blocking period (Figure 4f), while class 7 accommodates two episodes of the end of storm track IOP 6 cyclone, remaining in the warm side of the jet stream (Figure 4g). The rearward (anticyclonic) wave breaking and filamentation characterizing the LC1 example are seen for classes 6 and 7.

The cyclonic family, which groups together classes 1, 2, and 3 (Figures 4a, 4b, and 4c), displays a warm TLS pattern tilted northwest-southeast, and quite cyclonically for classes 2 and 3 (Figures 4b and 4c). Thus the upper level structure is characterized by forward (cyclonic) trough roll up as the typical LC2. The classes are mostly populated by rain events occurring in February. Fronts are the largest events in class 1 with the rain area located around 40°N (Figure 4a). Class 2 is populated notably by some end of storm track cases (IOP 19, IOP 12, LOP1, LOP 2). Class 3 is populated notably by some large-scale baroclinic cases (IOP 9, 14, and 17) with the rain area located between 40°N and 50°N. These cases are typical of the Norwegian cyclones that mimic the LC2 example.

Even if the period of study is limited in time, it is remarkable that the classification can discriminate rain events both between different weather regimes and between different kinds of weather system. Thus the cyclonic family groups cases that occurred during the zonal regime, in particular all the large-scale baroclinic systems, whereas the anticyclonic family groups blocking regime cases, which are mostly frontal systems. Moreover, it is suggested that composite classes associated with blocking and zonal regimes lead to preferential baroclinic life cycles that mimic the idealized LC1 and LC2 paradigms, respectively.

4. Conclusion

Physical parameters retrieved from TOVS measurements are used to study the large-scale cloud, precipitation, and lower stratosphere characteristics in the North Atlantic during the FASTEX period in January and February 1997. The following physical parameters are examined: temperature of lower stratosphere, cloud top pressure, and precipitation index under the guidance of the SSM/I observations.

These dynamically consistent (i.e., temporally and spatially collocated) fields are able to characterize the three weather regimes occurring during FASTEX. Thus the mean distributions of these satellite-retrieved parameters are organized in locations expected from the cyclonic activity. The Hovmöller diagrams give further details on the organization. High-level cloud patterns, when accompanied by low values of normalized ΔMSU, can be discriminated with respect to TLS field. When no (or weak) warm TLS feature can be found upstream, such patterns are frontal systems. On the contrary, a warm TLS event present upstream of a rainy cloud feature suggests a baroclinic interaction. In this case, the high-level cloud pattern is associated with a large-scale baroclinic cyclone, or at least a mature low.

When examining the most precipitating cases using the composite technique, the nondeveloped class (in terms of absence of high-cloud cover) is characterized by the absence of warm TLS features, grouping mostly blocking-regime cases.

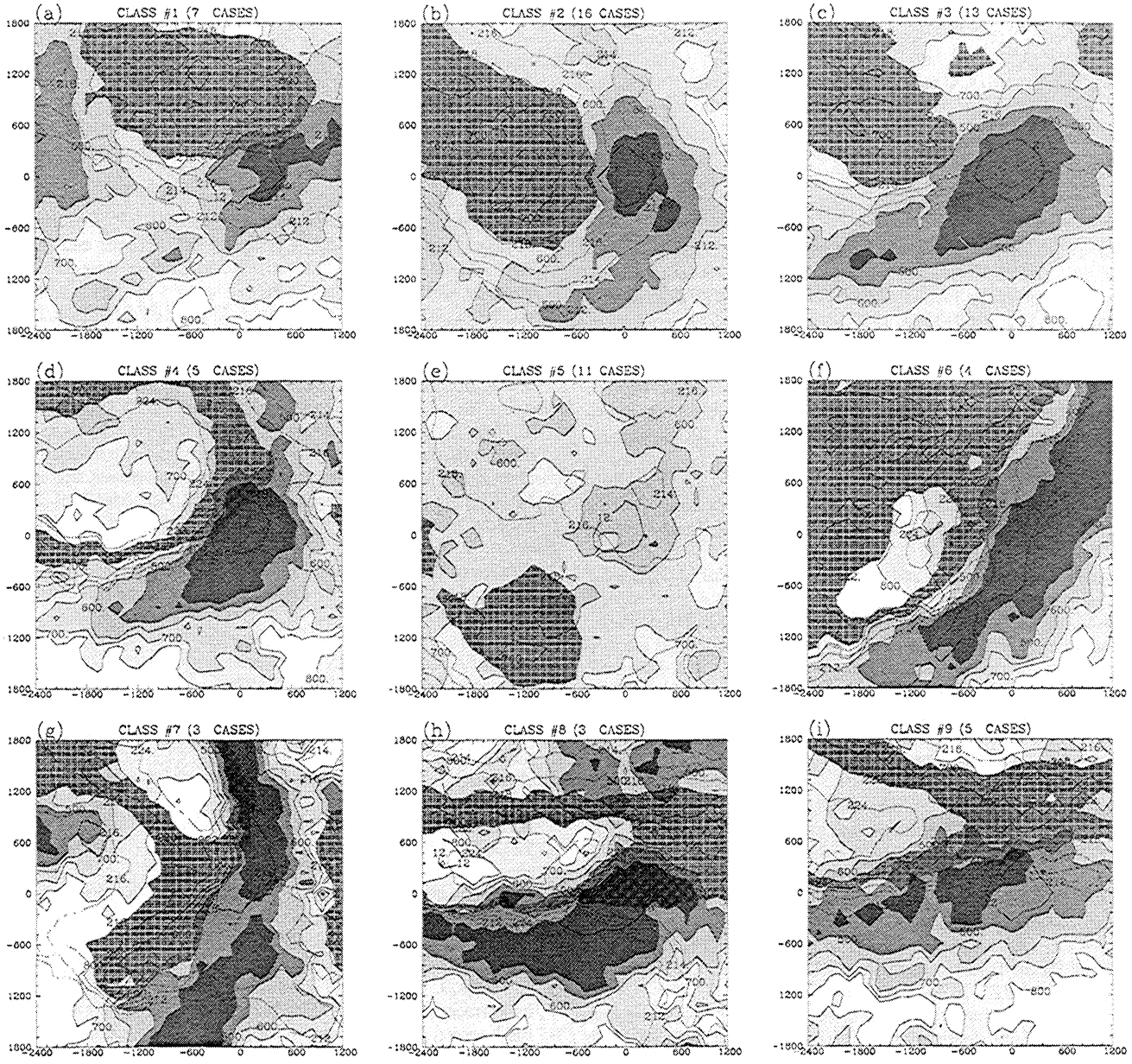

Figure 4. Composite views of the nine classes with the precipitation area in bold solid line (normalized ΔMSU< 12 K), the cloud top pressure in solid lines every 100 hPa, and TLS in dashed line every 2 K. The shading indicates cloud top pressure (dark gray, pressure over 400 hPa; medium gray, pressure between 500 and 400 hPa, etc.) and the dashed patterns indicates TLS between 218 and 222 K.

On the other hand, the cases that are well developed in term of cloud cover are characterized by warm TLS patterns upstream the precipitation area. This result obtained with satellite observations confirms the finding of a previous study using model analysis [*Baehr et al.*, 1999]. Moreover, the well-developed cases could be grouped into three families depending on the orientation of the warm TLS features: zonal, anticyclonic, and cyclonic. Only the later family, characterized by a cyclonically tilted trough, clusters the large-scale baroclinic systems that all occurred during the zonal regime. This suggests that a cyclonically tilted trough has a positive impact on the development of cyclones.

We plan to extend such a study to a longer period of time, to look at the variability from intraseasonal to interannual time scale (using reanalyzed TOVS data over the 1979-1999 period). Moreover, similar studies for more recent periods of time will benefit from the increased spatial and spectral resolutions of the recent instruments (in particular AMSU, the Advanced MSU now on board the NOAA satellites).

Acknowledgments. This research was supported by the FASTEX-Cloud System Study Project funded by the European Commission under contract ENV4-CT97-0625. Computer resources were alloted by IDRIS (projects 97569, 98569, and

981076). Retrievals used here have been obtained from the Atmospheric Radiation Analysis group at LMD, through the NOAA/NASA TOVS Pathfinder (Path-B) program. The SSM/I data come from the NOAA Satellite Active Archive. Thanks are due to the anonymous reviewers for comments on the manuscript.

References

Ayrault, F., and A. Joly, Une nouvelle typologie des dépressions météorologiques, classification des phases de maturation, *C. R. Acad. Sci., Ser. IIa, 330,* 167–172, 2000.

Baehr, C., B. Pouponneau, F. Ayrault, and A. Joly, Dynamical characterization of the FASTEX cyclogenesis cases, *Q. J. R. Meteorol. Soc., 125,* 3469–3494, 1999.

Charney, J. G., The dynamics of long waves in a baroclinic westerly current, *J. Meteorol., 4,* 135–162, 1947.

Chédin, A., N. A. Scott, C. Wahiche, and P. Moulinier, The Improved Initialization Inversion method: A high resolution physical method for temperature retrievals from the TIROS-N series, *J. Clim. Appl. Meteorol., 24,* 124–143, 1985.

Claud, C., K. B. Katsaros, N. M. Mognard, and N. A. Scott, Synergetic satellite study of a rapidly deepening cyclone over the Norwegian Sea: 13-16 February 1989, *Global Atmos. Ocean Syst., 3,* 1–34, 1995.

Eady, E. T., Long-waves and cyclone waves, *Tellus, 1*(3), 33–52, 1949.

Fourrié, N., C. Claud, J. Donnadille, J.-P. Cammas, B. Pouponneau, and N. A. Scott, The use of TOVS observations for the identification of tropopause-level thermal anomalies, *Q J. R Meteorol. Soc., 126,* 1473–1494, 2000.

Gelaro, R., R. H. Langland, G. D. Rohaly, and T. E Rosmond, An assessment of the singular-vector approach to targeted observing using the FASTEX dataset, *Q. J. R. Meteorol. Soc., 125,* 3299–3327, 1999.

Hoskins, B. J., M. E. McIntyre, and R. W. Robertson, On the use and significance of isentropic potential vorticity maps, *Q. J R. Meteorol. Soc., 111,* 877–946, 1985.

Joly, A., et al., The Fronts and Atlantic Storm Track Experiment (FASTEX): Scientific objectives and experimental design, *Bull. Am. Meteorol. Soc., 78,* 1917–1940, 1997.

Joly, A., et al., Overview of the field phase of the Fronts and Atlantic Storm Track Experiment (FASTEX) project, *Q. J. R. Meteorol. Soc., 125,* 3131–3163, 1999.

Koehler, T L., Limb correction effects on TIROS-N Microwave Sounding Unit observations, *J. Appl. Meteorol , 28,* 807–817, 1989.

Kucharski, F., and A. J. Thorpe, Upper-level barotropic growth as a precursor to cyclogenesis during FASTEX, *Q. J. R. Meteorol. Soc., 126,* 3219–3232, 2000.

Kucharski, F., and A. J. Thorpe, The influence of transient upper-level barotropic growth on the development of baroclinic waves, *Q. J. R. Meteorol. Soc., 127,* 835–844, 2001.

Kummerow, C. D., and L. Giglio, A passive microwave technique for estimating the vertical structure of rainfall from space, I, Algorithm description, *J. Appl. Meteorol., 33,* 3–18, 1994.

Langland, R. H., R. Gelaro, G. D. Rohaly, and M. A Shapiro, Targeted observations in FASTEX: Adjoint-based targeting procedures and data impact experiments in IOP17 and IOP18, *Q. J. R Meteorol. Soc., 125,* 3241–3270, 1999.

Lorenz, E. N., Effects of analysis and model errors on routine weather forecasts, in *Proceedings of ECMWF Seminars on Ten Years of Medium-Range Weather Forecasting*, vol. 1, pp. 115–128, Eur. Cent. for Medium-Range Weather Forecasts, Reading, England, 1990.

Phillips, N. A., Cloudy winter satellite retrievals over the extratropical Northern Hemisphere oceans, *Mon. Weather Rev., 109,* 652–659, 1980.

Rossow, W. B., A. W. Walker, D. Beuschel, and D. Roiter, International Satellite Cloud Climatology Project (ISCCP): Description of new cloud datasets, Int. Counc. of Sci. Unions and WMO Rep. *WMO/TD-No 737,* 115 pp., World Climate Research Programme, Geneva, February 1996.

Scott, N. A., A. Chédin, R. Armante, J. Francis, C. Stubenrauch, J.-P. Chaboureau, F. Chevallier, C. Claud, and F. Chéruy, Characteristics of the TOVS Pathfinder Path-B dataset, *Bull. Am. Meteorol. Soc., 80,* 2679–2702, 1999.

Shapiro, M. A., H. Wernli, J.-W. Bao, J. Methven, X. Zou, J. Doyle, T. Holt, E. Donald-Grell, and P. Neiman, A planetary-scale to mesoscale perspective of the life cycles of the extratropical cyclones, in *The Life Cycles of Extratropical Cyclones*, edited by M. A. Shapiro and S. Gronås, pp. 139–186, Am. Meteorol. Soc., Boston, Mass., 1999.

Shapiro, M. A., H. Wernli, N. A. Bond, and R. Langland, The influence of the 1997-1999 ENSO on extratropical baroclinic life cycles over the eastern North Pacific, *Q. J. R Meteorol. Soc., 80,* 331–342, 2001.

Smith, W. L., H. M. Woolf, C. M. Hayden, D. Q. Wark, and L. M. McMillin, The TIROS-N operational vertical sounder, *Bull. Am Meteorol. Soc., 60,* 1177–1187, 1979.

Spencer, R. W., Global oceanic precipitation from the MSU during 1979-91 and comparisons to other climatologies, *J. Clim., 6,* 1301–1326, 1993

Stubenrauch, C. J., W. B. Rossow, F. Chéruy, A. Chédin, and N. A. Scott, Clouds as seen by infrared sounders (3I) and imagers (ISCCP), I, Evaluation of cloud parameters, *J. Clim., 12,* 2189–2213, 1999a.

Stubenrauch, C. J., A. Chédin, R. Armante, and N. A. Scott, Clouds as seen by infrared sounders (3I) and imagers (ISCCP), II, A new approach for cloud parameter determination in the 3I algorithms, *J. Clim., 12,* 2214–2223, 1999b.

Szunyogh, I., Z. Toth, K. A Emanuel, C. H. Bishop, C. Snyder, R. E. Morss, J. Woolen, and T. Marchok, Ensemble-based targeting experiments during FASTEX: The effect of dropsonde data from the Lear jet, *Q. J. R. Meteorol. Soc., 125,* 3189–3217, 1999.

Thorncroft, C. D., B. J. Hoskins, and M E. McIntyre, Two paradigms of baroclinic-wave life-cycle behavior, *Q. J. R. Meteorol. Soc., 119,* 17–55, 1993.

J.-P. Cammas, J.-P. Chaboureau, and P. J. Mascart, Laboratoire d'Aérologie, Observatoire Midi-Pyrénées, 14 av. E. Belin, 31400 Toulouse, France. (camjp@aero.obs-mip.fr; chajp@aero obs-mip.fr; masp@aero.obs-mip.fr)

C. Claud, Laboratoire de Météorologie Dynamique, École Polytechnique, 91128 Palaiseau Cedex, France. (claud@lmd.polytechnique.fr)

(Received November 13, 2000; revised March 8, 2001; accepted March 21, 2001.)